# The CCAT 25 m diameter submillimeter-wave telescope

David Woody*[a], Steve Padin[b], Eric Chauvin[c], Bruno Clavel[c], German Cortes[d], Andy Kissil[e], John Lou[e], Paul Rasmussen[a], David Redding[e] and Jeff Zolkower[d],

[a]Owens Valley Radio Observatory, Caltech, 100 Leighton Lane, Big Pine, CA, USA 93513-0968; [b]Caltech, Pasadena, CA, USA; [c]Eric Chauvin Consulting, Pasadena, CA, USA; [d]Cornell, Ithaca, NY, USA; [e]JPL, Pasadena, CA, USA

## ABSTRACT

CCAT will be a 25 m diameter telescope operating in the 2 to 0.2 mm wavelength range. It will be located at an altitude of 5600 m on Cerro Chajnantor in Northern Chile. The telescope will be equipped with wide-field, multi-color cameras for surveys and multi-object spectrometers for spectroscopic follow up. Several innovations have been developed to meet the <0.5 arcsec pointing error and 10 μm surface error requirements while keeping within the modest budget appropriate for radio telescopes.

**Keywords:** Telescopes, optics, telescope structures, telescope mounts, telescope surface control

## 1. INTRODUCTION

CCAT will be a 25 m diameter telescope, operating in the 0.2 to 2 mm wavelength range. It will be located at an altitude of 5600 m on Cerro Chajnantor in Northern Chile, near ALMA. This is one of the best submillimeter sites on Earth.[1,2] This paper describes the design features of the telescope developed to meet the demanding requirements for a radio telescope operating at short submillimeter wavelengths.

CCAT will be equipped with wide-field, multi-color cameras for surveys, and multi-object spectrometers for spectroscopic follow up. It will observe structures on all scales ranging from Kuiper Belt objects to clusters of galaxies, but its immediate impact is likely to be in tracing the process of galaxy formation from the first giant starbursts. The large 1° field of view (FoV) will be covered using sub-field cameras. This allows the first light instrument to be modest sized (few x10k pixels at 350 μm) with later additions to fill the full FoV. CCAT will be sensitive with the first light instruments reaching the $5\sigma$ confusion limit in a few hundred hours of observing time. The 1 deg$^2$ image will contain tens of thousands of submillimeter galaxies at redshift ~2, and a few strongly lensed galaxies at redshift >6.3.[3,4] Photometry in a few bands will yield rough estimates of the redshifts of these objects, but a multi-object spectrometer (MOS) will clearly be needed for follow up. CCAT will eventually be equipped with cameras covering all the atmospheric windows in the $\lambda$ = 0.2 to 2 mm range, with a FoV up to 1°, and an MOS that can select tens of objects from the 1° FoV.

The optical design developed to provide high efficiency over the full 1° deg FoV is described in section 2. The primary reflector and support structure are described in section 3. This section also describes the sensors and control system for maintaining the surface figure between infrequent wave front measurements. The secondary and tertiary are described in section 4. The mechanical design of the mount and drive system and pointing are presented in section 5. A summary of the design features and expected performance are given in section 6.

## 2. OPTICAL DESIGN

CCAT is a wide-field Gregory telescope with cameras and spectrometers at both Nasmyth foci.[5,6] All the CCAT instruments will be available all the time, switching between instruments will be done by changing the pointing and rotating the tertiary mirror. This approach minimizes instrument changes, which is an advantage for a remote site.

* dwoody@caltech.edu; phone 1 760-938-2075x111; fax 1 760-938-2075; http://www.ccatobservatory.org

Ground-based and Airborne Telescopes IV, edited by Larry M. Stepp, Roberto Gilmozzi, Helen J. Hall,
Proc. of SPIE Vol. 8444, 84442M · © 2012 SPIE · CCC code: 0277-786/12/$18 · doi: 10.1117/12.925229



Downloaded From: http://proceedings.spiedigitallibrary.org/ on 01/24/2013 Terms of Use: http://spiedl.org/terms

At short submillimeter wavelengths, the transmission of the atmosphere is only ~50%, so there is little to be gained by building a telescope with very low emissivity. CCAT is therefore an on-axis telescope with a total emissivity of ~9% (3% from the reflectivity of the mirror surfaces, 2% from the secondary, 2% from the secondary support, and 2% from gaps between reflector tiles).

CCAT has a primary focal ratio of f/0.4, so the volume swept out by the telescope is limited by the diameter of the primary. This minimizes the size and cost of the enclosure, which is important because the cost of the enclosure is large (~1/4 of the cost of the telescope) and it scales at least with surface area.

CCAT will spend much of its time on surveys, so survey speed is an important consideration. The optical design of CCAT is therefore optimized for wide FoV. At mm wavelengths, the FoV is limited to ~1deg by the strong curvature of the focal surface. 1° FoV is a fairly hard limit and it sets the final focal ratio of the telescope in order to pass the beam from the secondary through a hole in the primary that is no larger than the secondary as shown in the upper left panel in Figure 1. For CCAT, the final focal ratio is f/6, which is considerably faster than many existing telescopes. The fast final focus allows a fairly simple relay to generate an ~f/3 beam to feed the detectors, but it moves the instruments close to the tertiary[6]. Table 1 gives the basic optical parameters for CCAT.

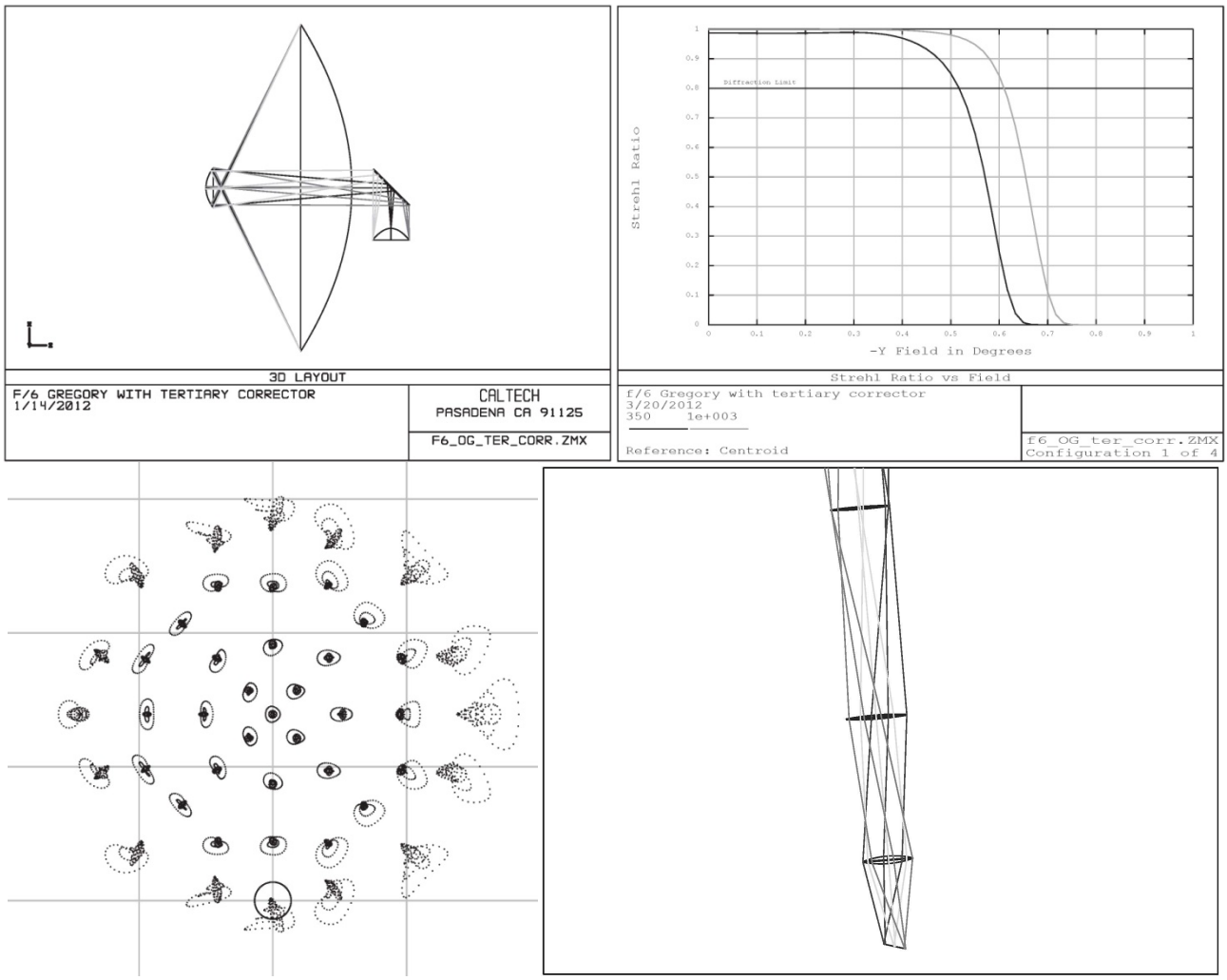


Figure 1. Optical layout of CCAT (top left), Strehl ratio vs. field radius (top right), full field spot diagram (bottom left) and relay details for a sub field camera with 5' fov (bottom right). In the full field spot diagram, the circle is the Airy disc at lambda=350um and the spots are magnified 50x. The sub field camera uses high density polyethylene lenses which are small in order to keep the total loss below ~20%. Much larger sub fields can be used if the lenses are made of Si.



Downloaded From: http://proceedings.spiedigitallibrary.org/ on 01/24/2013 Terms of Use: http://spiedl.org/terms

Table 1. Optical parameters for CCAT.

| Parameter | Value |
|---|---|
| Primary diameter | 25 m |
| Primary focal ratio | 0.4 |
| Final focal ratio | 6 |
| Back focal distance | 6.1 m |
| Primary to secondary separation | 11.15 m |
| Secondary to tertiary separation | 14.15 m |
| Field of view | 1° |

The secondary is 3 m diameter, strongly curved, and its surface must be set within ~2 μm RMS. This presents a significant challenge because direct mechanical measurements, e.g., with a coordinate measuring machine (CMM), cannot achieve the required accuracy. An optical measurement must be used, and this is much easier if the secondary is concave. CCAT is therefore a Gregory telescope in order to allow measurements of the surface profile of the secondary using millimeter wave holography[7,8].

At the shorter submillimeter wavelengths, aberrations are important, so the FoV can be increased by adding a corrector. In CCAT, the correction is done at the tertiary. This not ideal, because the tertiary is not a constant distance from the focal surface, but Figure 1 shows that good wide field performance can be obtained, and since the tertiary is made of machined aluminum tiles, it does not cost much to implement a complicated profile. To maximize the Strehl ratio over the field, the conic constants of the primary and secondary are also adjusted slightly from the nominal values for an aplanatic design. The CCAT primary will be cut as a paraboloid and the tiles set to the required profile when the segments are assembled.

It is impractical to build relay optics for the full 1° FoV of CCAT, so the field must be broken up into smaller pieces. The field selection must be done at a focus, where beams from adjacent fields do not overlap. This leads to the sub-field camera approach shown in Figure 1, where the refractive relay fits within the cylinder defined by the field lens. Reflective sub-field camera schemes are also possible, but it is not easy to close-pack the mirrors.

## 3. PRIMARY

The accuracy requirement for the primary surface is <7 μm RMS under all operating conditions. The telescope will be inside an enclosure which will greatly reduce the wind loading and keep direct sunlight off the primary and its support structure. Even with this shielding, the required surface is better than can be achieved for a passive 25 m diameter radio telescope structure utilizing the best carbon fiber reinforced plastic (CFRP) material. CCAT will have an active primary surface consisting of 162 reflector segments mounted on three computer controlled actuators to give independent piston, tip and tilt control of each segment. A control system based on an innovative imaging displacement sensor (IDS) that measures the six degrees of freedom (DoF) displacements between neighboring segments will command the actuators to maintain the primary surface figure. To achieve the best passive performance and to improve the thermal stability, the support structure for the reflector segments and secondary mirror will be a carbon fiber reinforced plastic (CFRP) truss.

### 3.1 Segments

Figure 2 shows a schematic diagram of a primary segment. A segment consists of aluminum reflector tiles mounted on CFRP sub-frames. This compound segment design was the result of a study looking at the options for light weight segments appropriate for a large submillimeter-wave telescope.[9] The precision machining of the reflecting surface occurs on manageable ½ m x ½ m aluminum tiles. Machining accuracy of <2 μm RMS can be achieved on tiles this size with five point support. The tiles can be very light weight with an areal density of ~10 kg/m$^2$. The sub-frames are fabricated from CFRP providing good thermal stability and high stiffness. The coefficient of thermal expansion (CTE) is <0.5 ppm/C with uniformity better than ± 0.1 ppm/C. The sub-frames don't have to be manufactured with high accuracy which is a large cost savings. The overall segment accuracy is achieved by factory setting of the five adjusters supporting each tile using a CMM. This concept increases the complexity of the segments but overcomes many of the difficulties and risks associated with monolithic segments. It also allows the fabrication of segments as large as 2 m x 2 m that meet the CCAT specifications of less than 4 μm RMS segment error under all operating conditions. The



Downloaded From: http://proceedings.spiedigitallibrary.org/ on 01/24/2013 Terms of Use: http://spiedl.org/terms

increased size reduces the number of computer controlled actuators and the node density in the reflector support structure.

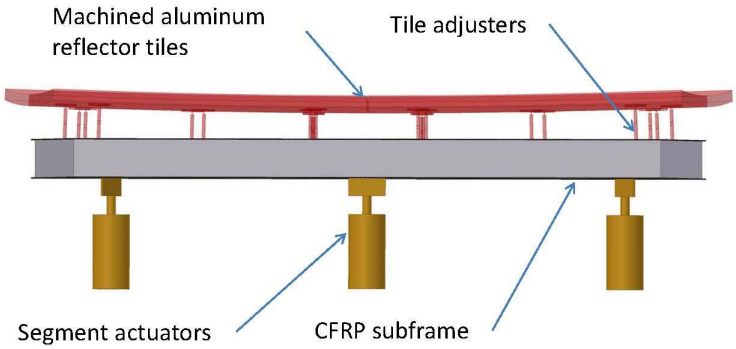


Figure 2. Schematic diagram of a primary segment.

The CCAT segmentation plan is shown in Figure 3. There are 162 segments in six rings with the segments sized to fit into a standard 2 m x 2 m x 1 m CMM. The layout avoids continuous radial lines which helps minimize the side lobes in the point spread function while also removing some of the degeneracy in the IDS configuration, improving the controllability of the surface.

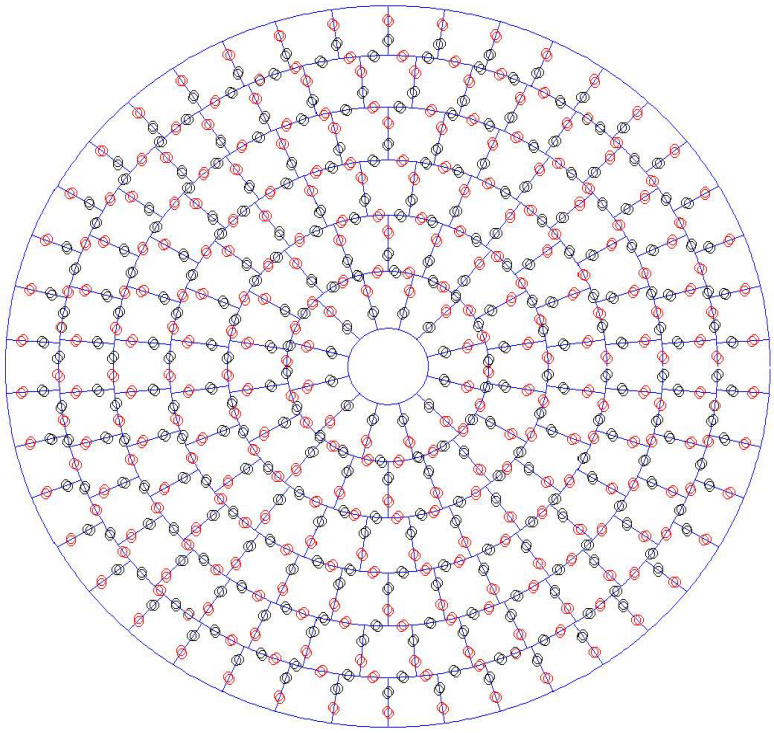

Figure 3. CCAT primary segmentation plan. The red and blue circles are the locations of IDSs.

The actuators and connection of the actuators to the CFRP sub-frames are designed to carry the full load of the segment in all orientations and under the -30 to +20 C temperature ranges with minimal distortion of the segment. The actuators will have an absolute precision of the better than ±1 μm over their 10 mm stroke and 0.1 μm readout and setting resolution.



Downloaded From: http://proceedings.spiedigitallibrary.org/ on 01/24/2013 Terms of Use: http://spiedl.org/terms

### 3.2 Support truss

The primary truss is constructed from struts with CFRP tubes and steel and Invar end-fittings and nodes. Figure 4 shows the truss structure including the secondary support structure. The truss has five layers of nodes with nine different classes of struts, one class for each node layer and a different class for struts interconnecting successive node layers. The large FoV and large instrument packages are accommodated by providing a 3 m diameter unobstructed cylinder through the structure along the elevation axis. The secondary support system is designed to have very low blockage while not compromising stiffness. The inner section of the support legs (green in Figure 4) are above the convergent cone of rays that meet at the prime focus and hence only block the plane wave incident on the aperture. The lower tripods (orange in Figure 4) connect to relatively stiff nodes in the primary support truss. This avoids having excessively long support legs with low net stiffness and resonant frequencies at the cost of a small amount of blockage of the rays converging towards prime focus.

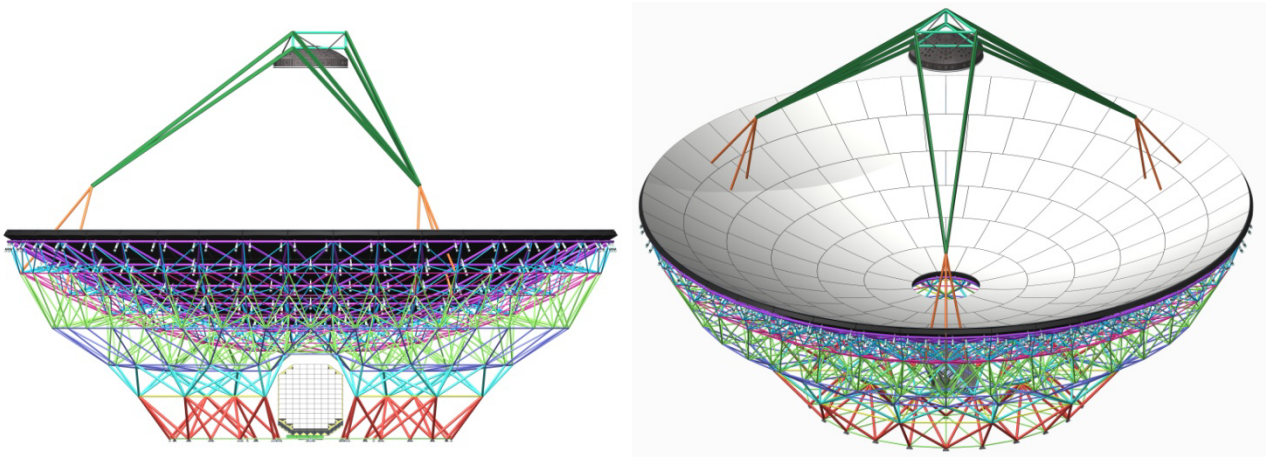

Figure 4. CCAT primary, secondary and tertiary. Left: side view along the elevation axis. Right: top front view.

One of the major challenges for CFRP telescope truss is the interface to the steel tipping structure which must allow for the differential thermal expansion of the two materials without distorting the primary surface or compromising the stiffness of the total structure. This is accomplished using the concept of thermal homology[10] which defines how multiple connections can be made between the CFRP and steel structures throughout a 3D volume without inducing thermal deformation stresses. The truss shown in Figure 4 has two concentric rings of blade flexures that connect the bottom set of nodes to the steel tipping structure plus a single rigid pillar at the center of the bottom layer. The blade flexures plus the radial CFRP struts connecting to the central pillar effectively constrain the bottom nodes in three DoF while allowing the steel tipping platform to expand relative to the central pillar. These added radial connections greatly improve the stiffness and resonant frequency of the primary support structure.

The nodes and end-fitting play a critical role in determining the performance of the CFRP truss. Figure 5 shows one end of a strut assembly. The metallic end-fittings and nodes dominate the effective CTE for the structure and can dominate the structural mass. In addition the ultimate strength of the truss will depend upon the bonding of the metallic fittings to the CFRP tubes. The design shown in Figure 5 has a few basic components which can be tailored for each strut end to accommodate the close packing at each node and are optimized to give the best stiffness to mass ratio. The CFRP tubes will have a negative CTE of ~ -0.3 ppm/C, depending upon the exact choice of material and layup, and the amount of Invar and steel in the end-fittings is adjusted to yield an effective CTE of 0.2 ppm/C from node-to-node for the various strut lengths which range from 0.8 to 3.8 m. Although the tailoring and optimization of each type of strut and node interface adds complexity to the design, the overall performance as measured by the mass and resonant frequency of the whole structure is significantly better than can be achieved using a common uniform end-fitting. The custom tailoring only requires adjusting the thickness of the steel spacers and setting the length of the threaded Invar studs.

The frequency of the lowest resonant mode was used as the evaluation parameter for the optimization of the structural design. The primary segments and secondary were treated as passive loads on a distributed structural spring. Following the formulation for a single mass on a distributed spring the resonant frequency can be written as



Downloaded From: http://proceedings.spiedigitallibrary.org/ on 01/24/2013 Terms of Use: http://spiedl.org/terms

$$f_0 = \frac{\beta}{\sqrt{1 + \frac{C_1 M_1 + C_2 M_2}{M_S}}}, \quad (1)$$

where $M_1$ and $M_2$ are the masses of the primary segments and the secondary reflector respectively and $M_S$ is the structural or spring mass. $\beta$ and the coefficients $C_1$ and $C_2$ are determined by fitting the FEA results for several configurations with different masses for the major components. $\beta$ is effectively the self-resonant frequency of the structure in the absence of any load from the primary segments or secondary and is a measure of the quality or stiffness-to-mass ratio for the structure. Knowing $C_1$ and $C_2$, Equation 1 can be used to calculate $\beta$ from the $f_0$ determine from the finite element analysis (FEA) of a given design. The design is optimized by varying the geometry and strut cross-sections to maximize $\beta$. Once the design has been optimized Equation 1 can be used to calculate the structural mass, $M_S$, required to meet a given $f_0$ requirement or to accommodate changes in the load masses while preserving $f_0$.

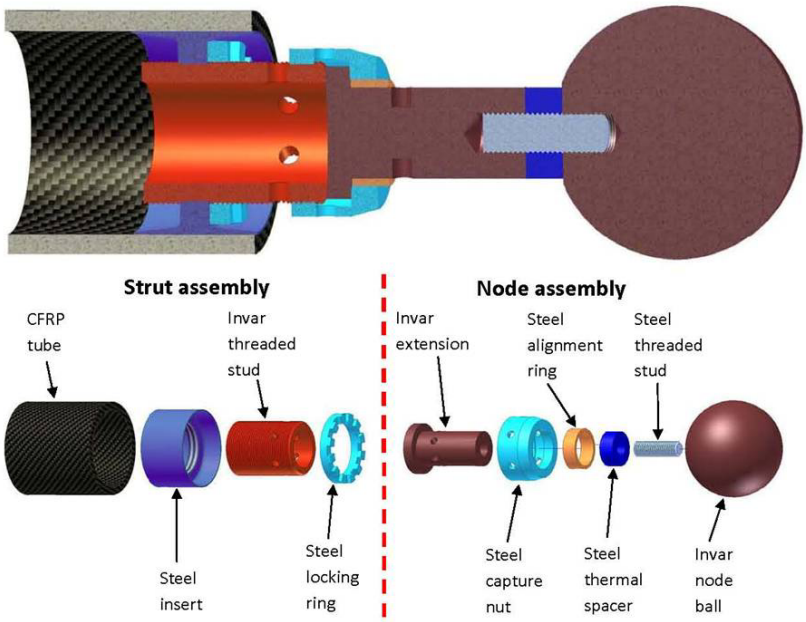


Figure 5. CCAT primary truss strut end assembly.

CFRP is an engineered material with a complex trade space for the fabricated tube elastic modulus, Y, CTE and cost. It can be a difficult task to optimize the performance per $. The self-resonant frequency $\beta$ of the structure will scale as $Y^{½}$ and this can be used in combination with Equation 1 to estimate the amount of CFRP required to achieve a given $f_0$ as a function of Y. This is then used in estimating the costs for fabricating the truss from different types of CFRP tubes.

The fast mapping requirement and high pointing accuracy requires a high $f_0$. The design goal for CCAT is $f_0$ ~10 Hz. Table 2 shows a sample set of material properties and masses for the primary, secondary and support truss. Table 3 summarizes the FEA results for this version of the CCAT primary and secondary under a variety of load conditions.

### 3.3 Surface control

The reflector segments will be mounted on computer controlled actuators. Although the primary structure is designed to have very small thermal distortions and perform well using lookup tables for gravity and large temperature changes, it is anticipated that active control of the surface based on a sensor system will be required to achieve the best performance at short submillimeter wavelengths. The sensor based active control strategy can also correct unanticipated or poorly characterized deformations in the mount, primary support structure, actuators and segment mounting.



Downloaded From: http://proceedings.spiedigitallibrary.org/ on 01/24/2013 Terms of Use: http://spiedl.org/terms

Table 2. Sample material and mass table for the CCAT primary and secondary.

| | | | | |
|---|---|---|---|---|
| Number of nodes | 517 | | | |
| Number of struts | 2880 | | | |
| | | | | |
| Structural material | Modulus [GPa] | Density [kg/m$^3$] | CTE [ppm/C] | Mass [kg] |
| steel | 210 | 7,850 | 11.4 | 1,500 |
| Invar | 141 | 8,000 | 0.9 | 1,200 |
| CFRP tubes | 140 | 1,850 | -0.5 | 7,000 |
| Strut assembly (average) | 141 | 2,472 | 0.2 | **9,700** |
| | | | | |
| Load masses | [kg/m$^2$] | | | |
| Segments + actuators | 30 | | | **16,000** |
| Secondary | 80 | | | **600** |
| | | | | |
| total | | | | **26,300** |

Table 3. FEA results.

| **Analysis case** | **FEA results** |
|---|---|
| Lowest resonance | 10 [Hz] |
| | RMS distortion |
| Z-gravity* | 112 [μm] |
| Y-gravity* | 218 [μm] |
| ΔT = 10 C temperature change | 0.1 [μm] |
| 0.1 ppm/C CTE random variation & 10C temperature change | 5.9 [μm] |
| ΔT = 1 C front-to-back , before focus correction | 3.1 [μm] |
| ΔT = 1 C front-to-back* | 0.2 [μm] |
| ΔT = 1 C top-to-bottom, before pointing correction | 1.5 [μm] |
| ΔT = 1 C top-to-bottom* | 0.1 [μm] |
| ΔT = ±0.5 C random in CFRP truss | 0.6 [μm] |
| ΔT = ±0.5 C random in steel axle structure | 6.7 [μm] |

*RMS distortion after correcting for focus and pointing

At millimeter and submillimeter wavelengths only the planets provide enough flux for a reliable wave front measurement with ~1 μm accuracy and even then it will take several hours to measure the surface at the ~1/2 m scale size required to accurately set each segment. Since the planets of the appropriate angular size and position in the sky will not always be available, the primary structure and any sensor or metrology system must have excellent stability over timescales of several months. An imaging displacement sensor (IDS) has been developed which utilizes a simple light emitting diode (LED) and pinhole collimator on one segment and a charge coupled device (CCD) camera on the neighboring segment to measure displacements in the plane normal to the collimator beam. By suitable placement of four such collimators and CCD cameras along an edge all six degrees of freedom motion between two segments can be measured with better than 0.1 mm accuracy. This sensor system is described in a companion paper at this conference.[11]

A state-control system has been developed and simulated to study the performance of the IDS sensor system for the full 162 segment CCAT surface. It uses the response matrix of IDS readings for all six DoF motion of each segment to estimate the system state from the sensor readings. The estimated state is projected to wavefront space using the response matrix to wavefront system state change. Actuator motions are computed and applied to minimize the wavefront error. The details of the control system are described in Redding et. al.[12,13] with the modeling and simulation results given in Lou et. al.[14] The simulations include expected gravity distortions of the primary support truss as well as applying random piston, tip and tilt displacements of the segments. After removing the six rigid body motions for the whole primary all 6x162-6 = 966 Eigen modes are measured with high fidelity. As expected, the weakest or poorest sensed Eigen modes mimic low order Zernike modes.



Downloaded From: http://proceedings.spiedigitallibrary.org/ on 01/24/2013 Terms of Use: http://spiedl.org/terms

Simulations of the performance of the control system have been analyzed under a variety of surface distortions. The simulations used the full model of the IDSs, including their locations and orientations on the segments, with a range of sensor noise levels. A simple characterization of the performance is the EMF (error multiplying factor), ratio of the RMS wave front error after applying control to the sensor noise. The expected EMF based on the Eigen values for all modes is ~10 which is also consistent with all of the simulations. Figure 6 shows the simulations using the gravity distortions predicted from FEA for the primary structure. The IDS system accurately predicts the large initial wavefront error of 489 μm RMS and the RMS wavefront after control of the three actuators on each segment is only 2 μm. Simulations using random motions in the six DoF of each segment give similar control performance.

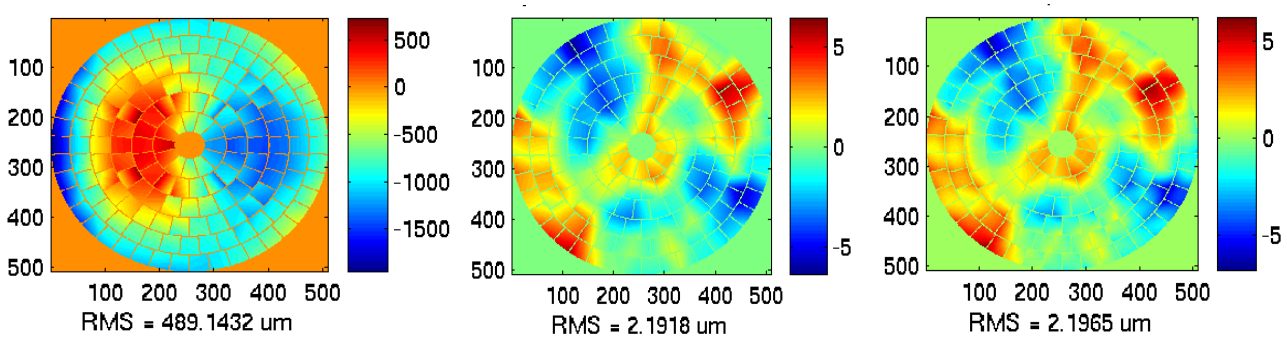


Figure 6. Control system simulation for FEA predicted gravity distortion at 0 deg elevation and 0.35 μm RMS sensor noise. Left: wave front for the gravity distortion. Center: difference between the initial wave front and the state estimated wave front determined from the IDS system. Right: resulting wave front after applying control to the segment actuators. The RMS values below each panel are the full wave front error.

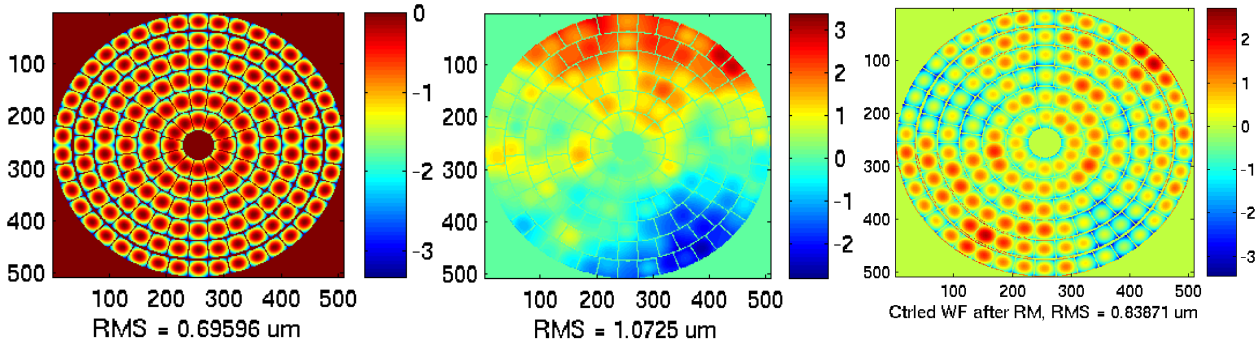


Figure 7. Control system simulation with 1 μm cupping on all segments and 0.07 μm RMS sensor noise. Left: wave front for the applied cupping distortion. Center: difference between the initial wave front and the state estimated wave front determined from the IDS system. Right: resulting wave front after applying control to the segment actuators. The RMS values below each panel are the full wave front error.

The more challenging case is a coherent or uniform distortion of all segments. Temperature gradients through the segments or sub-frames with slightly different CTE for the front and back face sheets can produce a change in curvature or cupping of the segments. To analyze this case a segment figure distortion proportional to $X^2+Y^2$ in the local segment frame was added as a seventh DoF for each segment in the IDS response matrix. The IDS system is able to measure the amount of cupping in each segment. Figure 7 shows the simulation for 1 μm of cupping applied to all segments. In this simulation the sensor noise was 0.07 μm (similar to the measured noise for the prototype IDS sensor in a single CCD image frame[11]). The state estimator accurately determined the cupping from the IDS readings consistent with the EMF and sensor noise. The control system successfully adjusted the piston of each segment to minimize the effect of the cupping despite the actuators not having the ability to change the curvature of the segments. Edge sensor systems that do not measure all six DoF displacements of a segment relative to its neighbor can actually amplify the cupping distortion across the surface, greatly increasing the wave front error.[9] The IDS and state control system also has good performance for random six DoF rigid body displacement of the segments along with random segment cupping distortions.



Downloaded From: http://proceedings.spiedigitallibrary.org/ on 01/24/2013 Terms of Use: http://spiedl.org/terms

## 4. SECONDARY AND TERTIARY

The secondary and tertiary mirrors use the same machined aluminum tile and sub-frame technology as the primary segments. Both mirrors are challenging, the tertiary because it is large (2.8 x 3.8 m), and the secondary because it is large and strongly curved (3 m diameter and 2.16 m radius of curvature at the apex). The secondary and tertiary sub-frames must have a CTE of a few x0.1±0.1 ppm/C in order to maintain its profile within a few μm rms with diurnal and annual temperature changes of ~20 C.

### 4.1 Secondary

The secondary has 3 rings of keystone-shaped tiles on a CFRP or Invar sub-frame. The tiling pattern is shown in the left panel of Figure 8. A CFRP sub-frame offers low mass, but maintaining low and uniform CTE for a strongly curved structure may be difficult. With a CFRP sub-frame, gravitational deformations of ~2 um rms require a ~0.3 m thick sub-frame. An Invar sub-frame may give a more uniform CTE, but Invar honeycomb material is only available up to 0.1 m thick, so a space frame support structure is needed. The secondary sub-frame is supported on a hexapod that is continuously adjusted to compensate gravitational deflection of the secondary support.

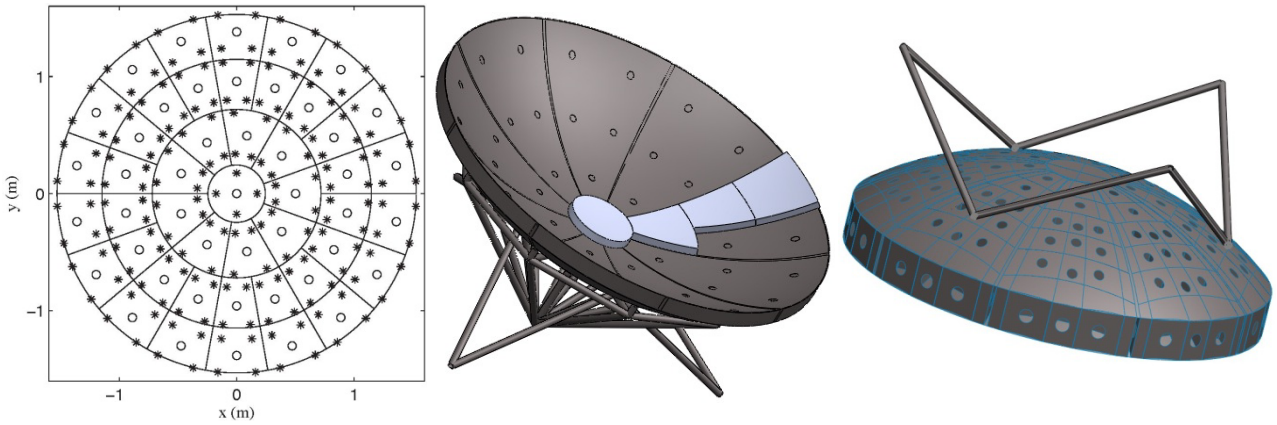


Figure 8. Secondary tiling pattern (left), Invar sub-frame (center) and CFRP sub-frame (right). Crosses and circles show the locations of tile adjusters on the sub-frame. Both subframes have 9 identical pie-shaped segments. The CFRP sub-frame has 6 mm thick face sheets and 3 mm thick ribs. The holes in the face sheets allow access to interior glue joints and to the tile adjusters.

### 4.2 Tertiary

The 1° field of view will project on the tertiary mirror as a 2.727 m x 3.856 m ellipse. The reflecting surface will be constructed of 105, ~0.29 m square aluminum tiles as shown in Figure 9. Each tile's surface will be uniquely machined to provide aberration correction. Each tile will be mounted on the CFRP sub-frame through a 5-point mounting arrangement on differential screw adjusters. The CFRP sub-frame will be ~0.3 m thick and will be constructed by a regular pattern of slotted intersecting ribs. The 3 mm thick ribs will be bonded to each other and to 3 mm top and bottom face sheets. The structure of the sub-frame core is closely coupled to the pattern of reflecting tiles on the mirror because the tiles must be attached at points where the core is stiff. The tiles have a radial support at the center, so this point is placed over the intersection of 2 ribs in the sub-frame core. The tile corner supports carry mainly axial loads, so these can be placed over a single rib, but close to an intersection of 2 ribs. Invar pads will be bonded to the rib core at all mounting points.

The sub-frame is supported on a steel space frame structure. Differential expansion between the low CTE, CRFP sub-frame and the steel space frame will be taken up by a set of blade flexures. The steel space frame will be attached to a rotator that will provide 180° of rotation in order to direct the optical beam to either Nasymth focus.



Downloaded From: http://proceedings.spiedigitallibrary.org/ on 01/24/2013 Terms of Use: http://spiedl.org/terms

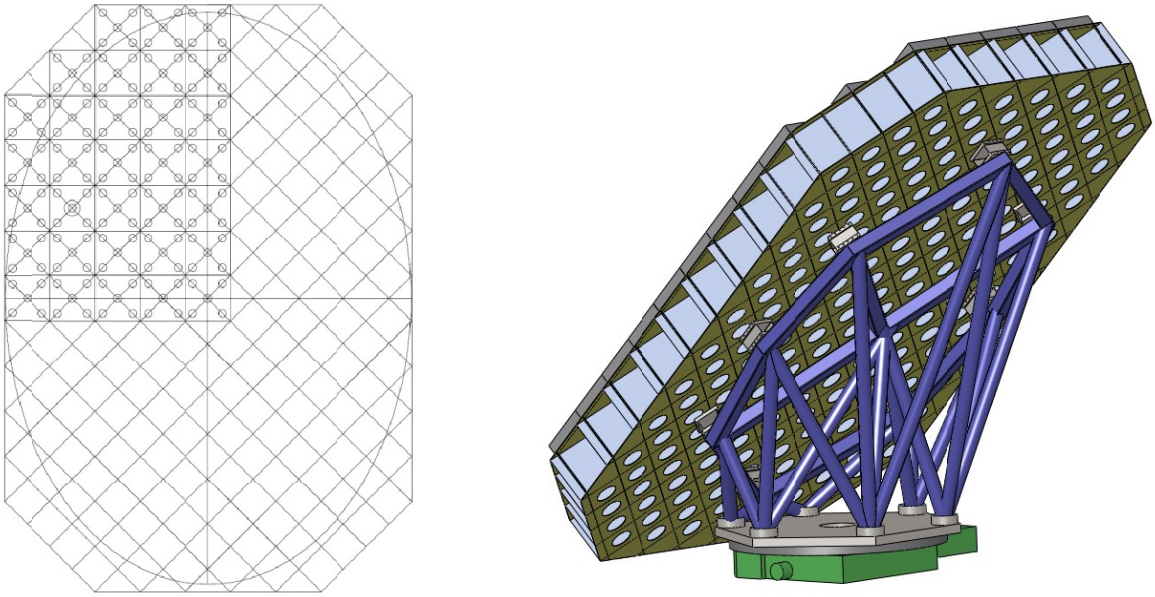

Figure 9. Left: Tertiary Mirror aluminum reflecting tile and sub-frame rib pattern. Right: Tertiary Mirror Assembly and Support Structure.

## 5. MOUNT AND POINTING

The critical specifications driving the mount design are the pointing, tracking accuracy and slew speed for wide field mapping.

### 5.1 Mount

The mount is an elevation over azimuth system designed to support and drive the primary, secondary, tertiary and scientific instruments as shown in Figure 10. The mount consists of an azimuth structure sitting on a stationary structure and supporting the elevation structure. The best pointing and tracking performance is achieved by using hydrostatic bearings (HSB), tape encoders and linear drives for both the elevation and azimuth axes.

Because of the size of the mount and the need for a large circular track for the azimuth HSB system, the azimuth structure is a traditional steel space-frame. This concept allows not only for a direct load path from the elevation structure to the foundation with beams working in tension and compression, but it also results in smaller and more manageable parts to ship to the site. A pintle bearing at the center of the track maintains the azimuth rotating structure on axis and accommodates the shear loads that may occur during seismic events. Similarly, a combination of a shell-design and a more traditional space-frame made of steel material and built as an extension of the truss of the primary appears the most appropriate for the elevation structure. This concept is compact enough to keep the mount naturally balanced around the elevation-axis despite the light weight of the primary.

The nominal diameter of the azimuth track is 20,225 mm, the height of the elevation-axis from the top of the azimuth track is 12,500 mm, the nominal distance between the elevation journals is 16,000 mm, the nominal diameter of the elevation journals is 5,400 mm, the inner diameter of the instrument rotators is 2,800 mm and the swept radius of the structures is 14,500 mm. The total mass of the telescope is 500,000 kg, the total mass of the azimuth rotating structure is 450,000 kg and the total mass of the elevation tipping mass is 200,000 kg, including the 35,000 kg primary, secondary and tertiary, 10,000 kg of instruments and 20,000 kg of equipment.

The HSB system uses master and slave pads. The master pads are fixed in position and arranged to create an iso-static system and the slave pads are free in position and are used to support the loads and to improve the dynamic performance without over constraining the system. There are six HSB pads for the azimuth track, four masters and two slaves. The elevation HSB system consists of two large elevation journals, one at each side of the mount, and four master HSB pads



Downloaded From: http://proceedings.spiedigitallibrary.org/ on 01/24/2013 Terms of Use: http://spiedl.org/terms

to carry the elevation rotating structure. To maintain the system in position and to accommodate the shear loads that may occur during seismic events, eight HSB pads are mounted laterally to the elevation journals; two master pads on one side and six slave pads on the other side, as shown in Figure 11. The operating pressure of the oil supply system is 100 bars with a total flow of 195 l/min at the highest temperature.

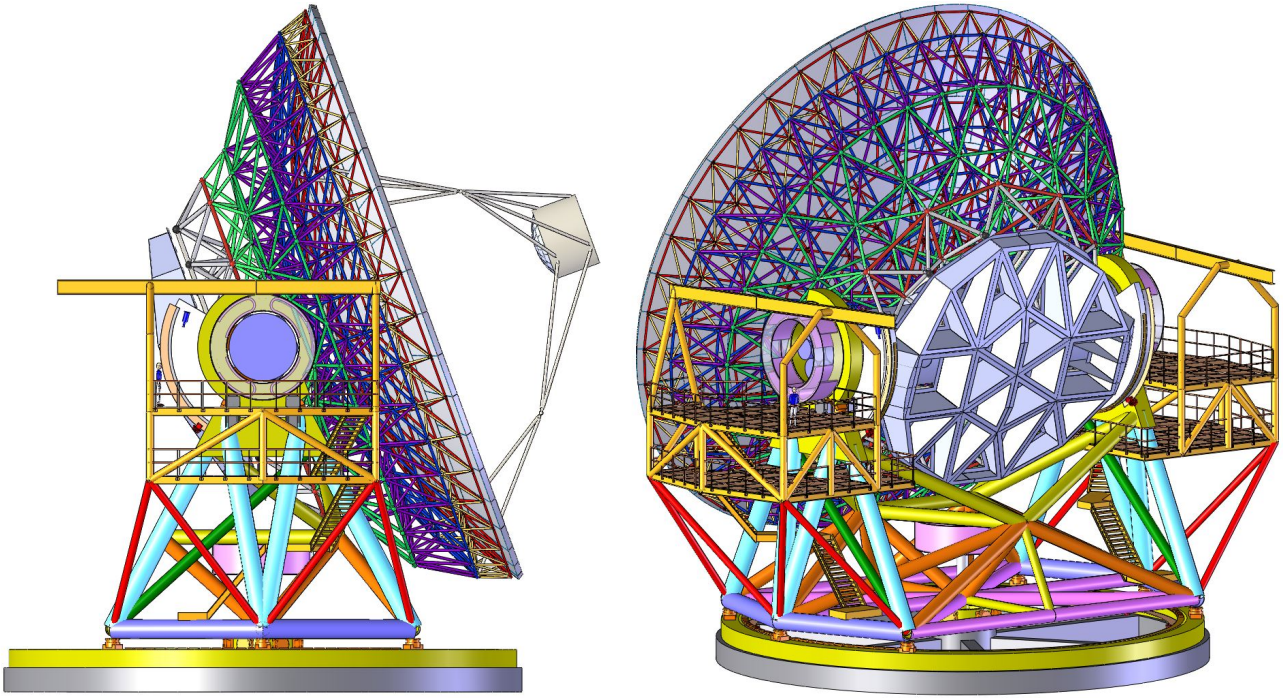

Figure 10. Side view (left panel) and rear view (right panel) of the CCAT telescope at 20 deg elevation limit. The primary truss and secondary are an earlier version compared to what is shown in Figure 4.

Two different styles of linear drives are used. The azimuth linear drive uses fixed passive magnetic on the inside of the track with 48 forcers on the azimuth structure. The flux lines are parallel to the azimuth axis. This allows the azimuth rotating structure to float laterally with a constant air gap between the magnets and the forcers without risking physical interferences that could occur during seismic events or under a difference of thermal expansion between the structures. The azimuth drive is capable of developing 1,150 kNm of nominal torque and to accelerate the mount at 2 deg/s$^2$. The elevation drive system consists of two large sectors of magnets mounted at both sides of the elevation structure and 18 radial flux forcers distributed between the elevation HSB pads at each side of the azimuth structure. In this configuration the elevation rotating structure can float laterally along the elevation-axis with a constant air gap between the magnets and the forcers without risking physical interferences during seismic events or thermal expansion between the structures. The elevation drive is capable of developing 200 kNm of nominal torque and to accelerate the mount at 2 deg/s$^2$. Both azimuth and elevation configurations allow the mounting surfaces of the HSB pads, magnets and forcers to be precisely machined, proof assembled and tested at the shop before shipping, like a single motor, so there are fewer alignment issues during installation at the site.

The mount design also includes the structures necessary for the installation and operation of the large instruments that will be used on CCAT. There are two Nasmyth platforms mounted at each side of the azimuth structure to provide access to the instruments inside the elevation tube and support ancillary equipment. The platforms are equipped with cranes designed to lift the instruments from the floor of the observatory to the top of the platforms. Motorized rotators, coaxial to the elevation-axis provide supports for the instruments at each side of the elevation structure. The rotators can be controlled to track the parallactic angle on the sky or to keep the instrument in a fixed gravity frame relative to the ground. The clear volume for instruments inside each rotator is 2.8 m diameter by 5 m long and can support as many as seven separate cryogenically cooled instruments. Essentially all of the machinery will be mounted on the azimuth structure with air and liquid heat exchangers to expel the heat to outside of the telescope enclosure. All rotating axes,



Downloaded From: http://proceedings.spiedigitallibrary.org/ on 01/24/2013 Terms of Use: http://spiedl.org/terms

azimuth, elevation and rotator will be equipped with chain style cable wraps to handle the necessary power cables, fluid lines, gas lines, vacuum lines and signal and control cables.

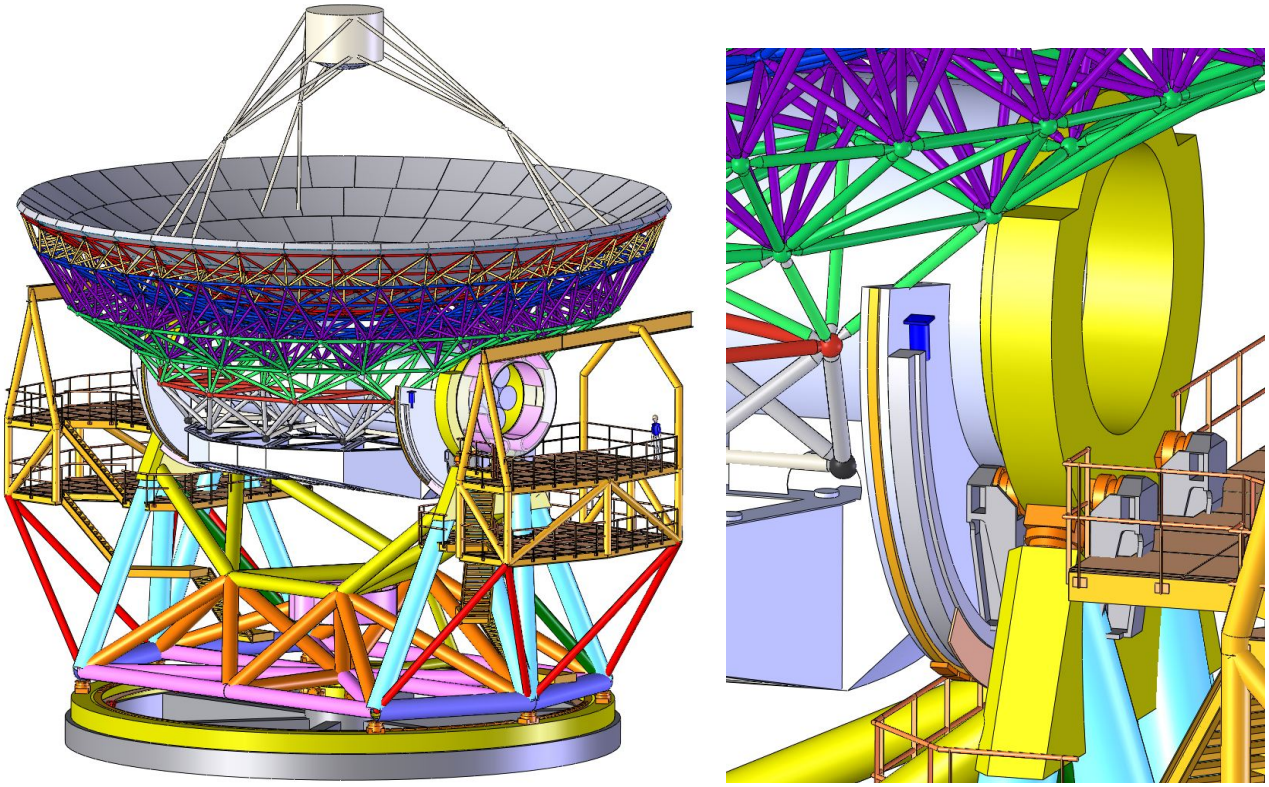

Figure 11. Left: front view of the telescope. Right: close up view of the elevation mechanical system.

Preliminary FEA has been performed to pre-optimize the mount and to determine the static and dynamic performance of the telescope. These analyses show that the azimuth structure is the main contributor to the lowest resonance frequencies of the telescope. The first resonance mode is a side-to-side sway at 4.8 Hz with most of the bending at the top of the azimuth structure that supports the elevation HSB pads. The second resonance mode is a fore-aft bending of the azimuth structure at 6.0 Hz and the third resonance mode is a twist around the azimuth-axis at 10.0 Hz. These modes are not directly sensed by the azimuth and elevation encoders. The analysis also shows that the elevation structure is very stiff with ±0.4 mm deviation from a plane at the interface between the mount and the primary truss as a function of elevation. The peak stresses of full structure are below the yield limit of the various materials even for a static 1 G of seismic acceleration in any direction.

### 5.2 Pointing

The pointing performance of CCAT is limited mainly by deflection of the CFRP primary truss when the telescope scans, thermal deformation of the steel mount, and thermal deformation of the CFRP secondary support. The pointing error (PE) due to deflection of the truss is PE ~ $\Omega/(2\pi f_0)^2$, where $\Omega$ is the angular acceleration of the truss and $f_0$ is the natural frequency. For CCAT, $f_0$ ~ 10 Hz and $\Omega = 0.3*(\lambda/350\ \mu m)deg/s^2$, so at $\lambda$ = 350 μm, PE ~ 0.3". This is essentially the entire 0.35"x($\lambda$ /350 um) pointing error budget, so a pointing correction must be applied based on the commanded or actual acceleration of the structure.

The ~10 K p-p diurnal air temperature variations at the CCAT site, combined with the different conductivities and heat capacities of the mount parts, cause ~0.1 C/hr changes in temperature gradient across the mount. The aspect ratio of the mount is ~1, so 0.1 C/hr change in temperature gradient causes pointing changes of ~0.2"/hr. A pointing measurement every ~1/2 hr is therefore required to meet the 0.35" pointing requirement at $\lambda$ =350 μm.



Downloaded From: http://proceedings.spiedigitallibrary.org/ on 01/24/2013 Terms of Use: http://spiedl.org/terms

The secondary support is made of CFRP with CTE ~ 0.5 ppm/C, so a typical 1 C temperature gradient across the structure causes a secondary decenter of ~6 μm. This corresponds to a pointing error of ~0.2". Temperature gradients inside the enclosure change on timescales of an hour, so a pointing measurement is required every ~1/2 hr.

Pointing errors due to thermal deformation of the mount and secondary support can be estimated based on measurements of the temperature of the structure. Such measurements should not be needed to meet the pointing requirements, but ~100 temperature sensors will be installed roughly uniformly over the CCAT structure.

## 6. SUMMARY

The basic environment parameters and observing parameters for CCAT are listed in Table 4. The telescope system design and various components are designed to meet the overall wavefront and pointing requirements for these operating conditions.

Table 4. Observatory parameters.

| Parameter | Value | Units | Notes |
|---|---|---|---|
| Wavelength | 350 | μm | |
| Mean outside wind speed | 6 | m/s | 3rd quartile (from submm.org) |
| Wind speed for pressure | 6.77 | m/s | $2^{1/2}(2/\pi)^{1/2}v_{outside}$, see CCAT-TM-56 |
| Density of air | 0.7 | kg $m^{-3}$ | At 5600 m altitude |
| Scan acceleration | 0.3 | deg $s^{-2}$ | $0.3°s^{-2}\times\lambda/350\mu m$ |
| rms temp gradient in dome | 1 | K | From TMT CFD |
| Soak temp change | 20 | K | Diurnal & longer (from submm.org) |
| Relative humidity change | 30 | % | Diurnal & longer (from submm.org) |
| Flux density of pointing source | 0.1 | Jy | For >1 source/$deg^2$, S<0.3Jy at λ=350μm and S<40mJy at λ=850μm, see Fig. 4.9 in feasibility study |
| Pointing integration time | 120 | s | < a few min for reasonable observing efficiency |
| Field angle | 0.30 | deg | |

The reflecting surfaces for the primary, secondary and tertiary will be precision machined light weight Al ~0.5 m x 0.5 m tiles. The reflector tiles are attached to CFRP frames by five manual adjusters. The frames provide a stiff and thermally stable structure for supporting the optical surface. The frames for the secondary and tertiary mirrors are kinematically attached to the telescope structure. In the case of the primary there are 162 ~2 m x ~2 m sub-frames which are mounted on three computer controlled actuators. The reflector tiles on the frames or sub-frames will be set in the factory or laboratory using a CMM or other metrology system.

The primary support structure is a truss consisting of CFRP tubes with Invar nodes and steel and Invar end-fittings. The metallic fittings are tailored for each strut end to produce an effective node-to-node CTE of 0.2±0.03 ppm/C while also maximizing the stiffness to mass ratio for the strut assemblies. The truss and secondary support structure are structurally very efficient, using only ~10,000 kg of structural mass to support ~16,000 kg of optics payload with a resonant frequency of ~10 Hz for the 25 m diameter telescope.

The active control of the primary surface uses a new type of IDS system that measures the full six DoF position of two segments relative to each other with an accuracy of better than 0.1 μm. The six DoF motion of the segments as well as a change in the radius of curvature of the segments are well sensed and the control system can maintain an RMS wave front error that is only ~10 times larger than sensor noise.

The mount will utilize hydrostatic bearings for both the azimuth and elevation axes. These axes will also use linear drives and tape encoders. This combination has very low friction and stiction with a very stiff drive closely coupled to the encoders. This will allow high bandwidth drive control and provide precision pointing with small tracking errors.

Table 5 gives the high level itemized error budget for CCAT. Each item in Table 5 is an RMS sum of many smaller component level errors. Note that three different options for the primary are given in Table 5; CFRP truss with open-loop control using lookup tables to control the actuators, steel truss using the IDS system for closed-loop control of the



Downloaded From: http://proceedings.spiedigitallibrary.org/ on 01/24/2013 Terms of Use: http://spiedl.org/terms

actuators and CFRP truss using the IDS system for closed-loop control. A steel truss running open loop misses the half wave front error (HWFE) by a large margin and is not included. The CFRP truss with open-loop control satisfies the basic HWFE requirement but with only a small margin while adding closed-loop control gives a significant margin and will produce significantly better Strehl ratios for observations through the 200 μm wavelength atmospheric window that is available from the Cerro Chajnantor site at 5600 m altitude.

Table 5. HWFE budget for reflector, pointing errors and emissity.

| Contribution | HWFE (μm rms) | PE (arcsec rms) | EM | Notes |
|---|---|---|---|---|
| Aberrations | 2.70 | 0.00 | | Gregory with tertiary corrector |
| Primary open-loop, CFRP truss | 8.83 | 0.05 | 0.019 | |
| Primary closed-loop, steel truss | 7.52 | 0.55 | | |
| Primary closed-loop, CFRP truss | 6.49 | 0.04 | | |
| Secondary | 6.17 | 0.31 | 0.053 | |
| Tertiary | 5.08 | 0.10 | 0.017 | |
| Instrument | 0.05 | 0.04 | | |
| Mount | 0.00 | 0.32 | | No HWFE from mount |
| Alignment | 2.19 | 0.10 | | Regular pointing with science camera, occasional wavefront measurements with WFS |
| Telescope total open loop, CFRP | 12.41 | 0.47 | 0.089 | |
| Telescope total closed-loop, steel | 11.51 | 0.72 | | |
| Telescope total closed-loop, CFRP | 10.87 | 0.47 | | |
| Telescope requirement | 12.50 | 0.35 | 0.100 | HWFE for <50% increase in integration time at λ=350μm, PE<1/10th beam, EM for <25% increase in integration time, from CCAT-TM-48 |
| Atmosphere | 5.74 | 0.23 | | 1st quartile |

## ACKNOWLEDGEMENTS

This work was supported by the John B. and Nelly Kilroy Foundation.

## REFERENCES

[1] Radford, S.J.E., et al., Submillimeter observing conditions on Cerro Chajnantor. Proc. SPIE. 7012 (2008).
[2] Giovanelli, R., et al., The Optical/Infrared Astronomical Quality of High Atacama Sites. II. Infrared Characteristics. PASP. 113: p. 10 (2001).
[3] Blain, A.W., et al., Submillimeter Galaxies. Phys. Rep. 369: p. 65 (2002).
[4] Negrello, M., et al., Astrophysical and cosmological information from large-scale submillimetre surveys of extragalactic sources. Mon. Not. R. Astron. Soc. 377: p. 11 (2007).
[5] Stacey, G.L., et al., Instrumentation for the CCAT telescope. Proc. Soc. Photo-Opt. Instrum. Eng. (2006).
[6] Padin, S., et al., CCAT Optics. Proc. SPIE. 7733: p. 77334Y-1-77334Y-11 (2010).
[7] Bennett, J.C., et al., Microwave holographic metrology of large reflector antennas. IEEE Transactions on Antennas and Propagation. AP-24(3): p. 295-303 (1976).
[8] Scott, P.F. and M. Ryle, A rapid method for measuring the figure of a radio telescope reflector. Monthly Notices of the Royal Astronomical Society. 178: p. 539-545 (1977).
[9] Woody, D.P., et al., Panel options for large precision radio telescopes. Proc. SPIE. 7018: p. 70180T1-70180T11 (2008).
[10] Woody, D.P., S. Padin, and T.A. Sebring, CFRP truss for the CCAT 25m diameter submillimeter-wave telescope Proc. SPIE. 7733: p. 77332B-1-77332B-10 (2010).
[11] Woody, D.P. and D.C. Redding, An Imaging Displacement Sensor with Nanometer Accuracy. Proc. SPIE. 8450 (2012).
[12] Redding, D.C., et al., Wavefront controls for a large submillimeter-wave observatory Proc. SPIE. 7733: p. 773329-1-773329-11 (2010).
[13] Redding, D.C. and e. al., Model-based Wavefront Control for CCAT. Proc. SPIE. 8339 (2011).
[14] Lou, J.Z., et al., Modeling a large submillimeter-wave observatory Proc. SPIE. 7733: p. 773326-1-773326-13 (2010).



Downloaded From: http://proceedings.spiedigitallibrary.org/ on 01/24/2013 Terms of Use: http://spiedl.org/terms